



Highly-resolved LES of turbulent convective flow along a PWR rod bundle

Djamel Lakehal

ASCOMP AG, Zurich, Switzerland

ARTICLE INFO

Article history:

Received 23 May 2017

Received in revised form 21 January 2018

Accepted 22 January 2018

Available online 20 February 2018

Keywords:

Pressurized Water Reactors

DNS

LES

Rod Bundle

ABSTRACT

A detailed numerical analysis of the turbulent convective flow along the heated rods of an idealized Pressurized Water Reactor (PWR) sub-channel is investigated using the CFD code TransAT. The flow is pretty much similar to circular pipe flow. Turbulent effects are predicted using highly-resolved Large-Eddy Simulation (LES) with a grid resolution of up to 6 million cells, resolving the viscous-affected layer. The sub-grid scale (SGS) viscosity produced by the model is indeed found to be of marginal effect for the grid and Reynolds number employed. Only first-order turbulence statistics are presented here. The results are discussed in detail, in particular key features specific to rod bundles, including low-Re effects in the narrow gap zone and the strong secondary flow motion, which is shown to exceed the turbulence counterpart (through the shear stress) near the wall. The secondary-flow motion induced by the mean flow is shown to be responsible for a large portion of the wall-to-flow heat transfer. The comparison of the LES results with existing DNS of pipe flow shows a very good agreement as to first-order statistics; higher-order statistics (including energy budgets) of the fluctuating fields have not been explored. A data basis has been generated for turbulence model comparison. Like in turbulent pipe flow, a physical explanation for the observed differences can be routed in the transverse curvature effects of the bundle geometry.

© 2018 Elsevier Ltd. All rights reserved.

1. Introduction

The onset of nucleate boiling on solid wall occurs when the temperature of the wall slightly exceeds saturation [1]. The small vapor bubbles form and stay attached to the solid wall. Past the point of net vapor generation, the bubbles detach and remain trapped within a layer relatively close to the wall, beyond which – towards the core flow – they condense. Under turbulent conditions, the flow will be further affected by large and small eddies, affecting in turn the rate of wall-to-core-flow heat transfer and thus phase change, both near the wall (boiling) and far in the core flow (condensation). The first objective of this exercise is to assess the performance of the ITM/CFD code TransAT [2] in predicting the turbulent convective flow upward along the heated rods of a PWR sub-channel. The key predicted quantity is the length at which the rod surface temperature reaches nucleation temperature, approximated here as the saturation temperature. For simplicity, we refer to it as the distance to the onset of nucleate boiling (X_{ONB}). Predicting this quantity correctly requires accurate prediction of turbulent flow, since the wall temperature is strongly dependent on the flow

structures, its unsteadiness and the rate of turbulent-stresses anisotropy. The problem is inspired by the PSBT (short for PWR Sub-channel and Bundle Tests) single sub-channel benchmark. The onset of nucleate boiling on the nuclear rod surface is one of many other complex mechanisms that pose challenges to the modellers [4]. Without listing all the features associated with turbulent flow in narrow gaps of sub-channels, it is perhaps useful to evoke the most important ones which the authors believe as key issues in modelling using mainstream CFD. The reader may refer to the review paper of Rehme [5] compiling early research findings on the subject, who has also noted the flow along a rod bundle is pretty much similar to circular pipe flow. Early experiments [6] revealed the existence of macroscopic pulsating flow structures (not necessarily turbulence) in the regions adjacent to the gaps, with strong implications on the mixing between adjacent sub-channels. This phenomenon was proved later on by Meyer [7]. Other important features were identified experimentally as marked characteristics of flow along rod bundles [8,9], including secondary flow motion and large-scale turbulent motions enhancing heat extraction from the heated wall.

Clearly, there are incentives to resort to 3D CFD for the prediction of the detailed fluid flow and temperature distribution in rod

E-mail address: Lakehal@ascomp.ch

bundles for safety issues and operational reliability of the fuel elements. Sub channel analysis ignores the fine structures of velocity and temperature distributions in the flow passages, and can thus not account for mixing effects caused by the presence of spacers or other geometrical disturbances. Large-scale turbulent motion and larger periodic pulsating structures responsible for mixing between sub-channels are out of reach of steady state approaches resorting to statistical averaged models [10]. Further, secondary flow motion could be predicted using anisotropic models (to a limited degree though) or full Reynolds stress models only. While the velocity magnitude associated with secondary flow moving within the elementary cells of the sub-channels maybe small (of the order of 10%) compared to the axial one, its implication on heat transfer is important, in particular near the wall, which appeals for the use of wall-resolved strategies. LES of turbulent flow along rod bundles are indeed rare in the literature, with the exception of the Japanese group [11–13] who produced several interesting contributions to the subject. Other contributions to the subject include the work of Merzari et al. [14] and Ninokata et al. [15].

We present the results of a LES and highly-resolved LES of turbulent convective flow upward along the heated rods of an idealized PWR sub-channel. The selected test-case is inspired by the PSBT single sub-channel benchmark [3], in terms of radial dimensions in particular, albeit the deliverables are different from the actual PSBT case. The focus here is on detailed flow profiles and temperature at the wall rather than on global parameters as required in the benchmark. The operating conditions selected here are made on purpose different from PSBT, namely the power, which has been adjusted according to the reduced length (1m instead of 3.65 m). The second objective is to provide a rich data basis to help assess the predictive performance of practical turbulence models to predict mean and RMS profiles, stresses and turbulent fluxes, wall temperature at which saturation conditions are reached.

2. Modelling

This work used the CFD code TransAT© developed at ASCOMP, which is a multi-scale, multi-physics, conservative finite-volume solver for single- and multi-fluid Navier-Stokes equations. The grid arrangement is collocated, and the solver is pressure based (Projection Type), corrected via density for compressible flows. Turbulent flows can be treated in two ways: RANS statistical models and Scale Resolving Approaches like LES and its DES and V-LES variants. LES is built within a dedicated version, with specific routines for pressure coupling, boundary conditions, diffusive fluxes and near-wall stress integration. A 2nd order implicit scheme is used for time marching. The solvers employed for pressure-velocity coupling include: GMRES, GMG & AMG, from the PETSc solver library. In LES the motion of the super-grid turbulent eddies is directly captured, whereas the effect of the smaller scale eddies is modeled or represented statistically by means of simple models, very much the same way as in Reynolds-averaged models (RANS); i.e. the usual practice is to model the sub-grid stress tensor by an eddy viscosity model. The code TransAT proved very efficient for LES and DNS problems [16].

2.1. Highly-resolved LES

A full DNS of this flow is difficult if one takes as reference published DNS of turbulent channel flow performed in Cartesian grids. The reasons are obvious: (i) the high Reynolds number typical to PWR's would require grids of hundreds (up to the billion) of million cells, in particular because the near-wall resolution is key in this context, and (ii), the complex bounding geometry implies

use of non-Cartesian grids, which add numerical diffusion to the discretization scheme, unless use is made of the Immersed Boundary Technique [12]. The resort to LES [17] is thus a pragmatic and defensible choice, but the meshing level or concentration may be an issue and has to be clarified first. Indeed, while a coarse mesh would not allow predicting a large portion of the structures, a very fine mesh could return results that are close to DNS in that the non-resolved eddy viscosity is marginally important; this is the essence of the so-called 'Highly-resolved LES', which applies as a simple definition to problems in which the ratio of eddy to molecular viscosity does not exceed 1.5–2, in comparison with conventional LES where this ratio should fall in the range 5–10. Other measures have been introduced, including comparing the subgrid-scale eddy viscosity to the resolved turbulence.

2.2. The filtered LES equations

In LES the motion of the super-grid turbulent eddies is directly captured whereas the effect of the smaller scale eddies is modeled or represented statistically by means of simple zero-equation models, very much the same way as in Reynolds-averaged models (RANS); i.e. the usual practice is to model the sub-grid stress tensor by an eddy viscosity model. In terms of computational cost, LES lies between RANS and DNS and is motivated by the limitations of each of these approaches. Since the large-scale unsteady motions are represented explicitly, LES is more accurate and reliable than RANS.

LES involves the use of a spatial filtering operation $\bar{F}(\mathbf{x}, t) = \int_{-\infty}^{\infty} F(\mathbf{x}', t) G(\mathbf{x} - \mathbf{x}') d\mathbf{x}'$, where the fluctuation of any variable $F(\mathbf{x}, t)$ from its filtered value is denoted by $f' = \bar{F} - F$. Filter function $G(\mathbf{x} - \mathbf{x}')$ is invariant in time and space, and is localized, and obeys the properties: $G(\mathbf{x}) = G(-\mathbf{x})$, and $\int_{-\infty}^{\infty} G(\mathbf{x}) d\mathbf{x} = 1$. Applying the filtering operation to the instantaneous Navier-Stokes equations under incompressible flow conditions leads to the system of filtered transport equations for turbulent convective flow (the equations are well known and are not repeated here), which involve the so-called SGS stress tensor and turbulent heat flux defined as:

$$\tau_{ij} \equiv \bar{\rho}(\bar{u}_i \bar{u}_j - \bar{u}_i \bar{u}_j); \quad q_j'' \equiv \bar{\rho}(\bar{T} \bar{u}_j - \bar{T} \bar{u}_j) \quad (1)$$

Only the deviatoric part of the SGS stress tensor is to be modeled using a statistical approach similar to RANS. This way, turbulent scales larger than the grid size are directly solved, whereas the effects of SGS scales are modeled.

2.3. SGS modeling

LES is based on the concept of filtering the flow field by means of a convolution product. The specific super-grid part of the flow with its turbulent fluctuating content is directly predicted whereas the sub-grid scale (SGS) part is modeled, assuming that these scales are more homogeneous and universal in behavior. For turbulent flows featuring a clear inertial subrange the modeling of the SGS terms in the statistical sense could thus safely borrow ideas from the RANS context, in particular use of the zero-equation model to mimic the momentum diffusive effects on the resolved field. Use is generally made of the Eddy Viscosity Concept, linking linearly the SGS eddy viscosity and thermal diffusivity to the gradients of the filtered velocity and temperature, respectively:

$$\tau_{ij} = -2\mu_{\text{sgs}} \bar{S}_{ij} + \frac{1}{3} \delta_{ij} \tau_{ll}; \quad \mu_{\text{sgs}} = (Cs\Delta)^2 \bar{\rho} |\bar{S}|^2 \quad (2)$$

$$q_j'' = -\alpha_\theta \frac{\partial \bar{T}}{\partial x_j}; \quad \alpha_\theta = \frac{\mu_{\text{sgs}}}{\text{Pr}_t}$$

The closure for the eddy viscosity above follows in general the Smagorinsky kernel model, linking the eddy viscosity to the square of a length scale and a time scale (the inverse of the second

invariant of the resolved rate of deformation tensor S_{ij}). The model constant (C_s) is either fixed or made dependent on the flow; this latter option is precisely the spirit of the dynamic model. A damping function is often introduced for the model constant C_s to accommodate the asymptotic behavior of near-wall turbulence. Similarly, the same strategy could be used to close the turbulent SGS heat flux, where the thermal diffusivity could be determined either based on the resolved thermal-flow field, or alternatively based on the eddy viscosity (defined dynamically) and a fixed turbulent Prandtl number. Using the first alternative means that the turbulent Prandtl number is not imposed but is a result of the model; this is known as the Dynamic Smagorinsky Model (DSM). The advantage of DSM compared the base model is that (i) the constant C_s may be negative, which does not exclude possible backscatter of energy, (ii) it returns the proper asymptotic behavior of the stresses near the wall with damping as required by the base model, and (iii) vanishes in laminar flow without *ad-hoc* intermittency functions.

Table 1

Reference operating conditions for PSBT tests [3].

Pressure	15.5 MPa
Saturation temperature	344.6 °C
Inlet temperature	290 °C
Mass flux	3333 kg/m ² s
Heat Flux	581 kW/m ²
Power	2.7 MW

Table 2

Test case 2 operating flow conditions.

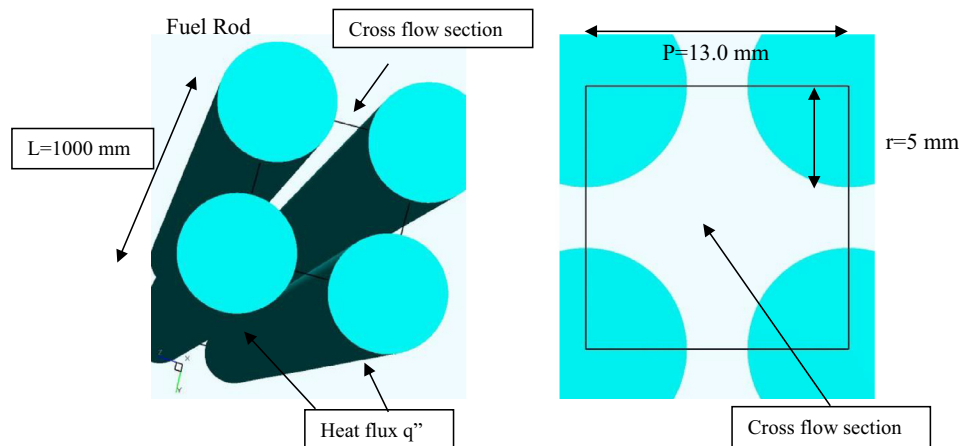
Pressure	15.5 MPa
Saturation temperature	344.6 °C
Inlet temperature	290 °C
Mass flux	74.1 kg/m ² s (or $Re_\tau = 300$)
Heat Flux	50 kW/m ²
Power	1.57 kW

The DSM approach is based on the application of a twice-larger filter width on top of the filtered Navier-Stokes equations. The details about the determination of the dynamic length scale for both the thermal and flow field are given by Moin et al. [18]. Many authors resorted with success to this particular SGS model, e.g. Peng and Davidson [19] and many others.

3. Problem description

The problem is inspired by the PSBT sub-channel benchmark [3] in terms of radial dimensions. Though the expected deliverables are different, the focus is on detailed flow and temperature profiles in the sub-channel, together with global parameters including the heat transfer coefficient, the onset of nucleation, the pressure drop and the thermal entry length. The operating conditions of the present case are made on purpose different from PSBT, namely the power and mass flow rate, which have been adjusted according to the reduced length (1 m instead of 3.65 m). The PWR fuel assembly consists of a rod bundle with water coolant flowing upward along the rods at a high Reynolds number. The rod diameter is 9.5 mm, the rod pitch is 12.6 mm and the active fuel length is typically ~ 3.7 m. The hydraulic diameter for a unit cell is $D_e = 11.8$ mm. The coolant pressure is 15.5 MPa with temperature ranging from 290 °C to 340 °C. Representative values of fluid properties are density: $\rho = 710$ kg/m³; dynamic viscosity: $\mu = 9 \times 10^{-5}$ Pa s; thermal conductivity: $\kappa = 0.54$ W/m-K; heat capacity: $C_p = 5.9$ kJ/kg-K. The mass flux is $G \sim 3700$ kg/m² s, corresponding to a Reynolds number $Re = GD_e/\mu \sim 4.8 \times 10^5$, shear velocity $u_\tau \sim 0.2$ m/s, and frictional Reynolds number $Re_\tau \sim 10^4$.

Several simplifications were adopted here: First, the temperature of nucleation is assumed to be equal to the saturation temperature; second, a configuration consisting of the flow along a single sub-channel with periodic conditions is assumed; third, since the shear Reynolds number for the PWR channel is $Re_\tau \sim 10^4$, performing DNS for such flow conditions would be computationally prohibitive. As such, the problem has been scaled down to more reasonable conditions, i.e. $Re_\tau = 300Re_\tau = 300$. Finally, the length

**Fig. 1.** Computational domain: Dimensions & BCs.**Table 3**

Grid properties used for the LES and for the highly-resolved LES.

$Re_\tau = 300$	Number of nodes		Resolution		Grid type	Total number of cells
	x-y	z	$\Delta x^+ - \Delta y^+$	N blocks		
Grid Med	40–40	798	0.5–2.1	208	BFC	1,317,400
Grid Fine	60–60	1600	0.4–1.5	832	BFC	6,011,200

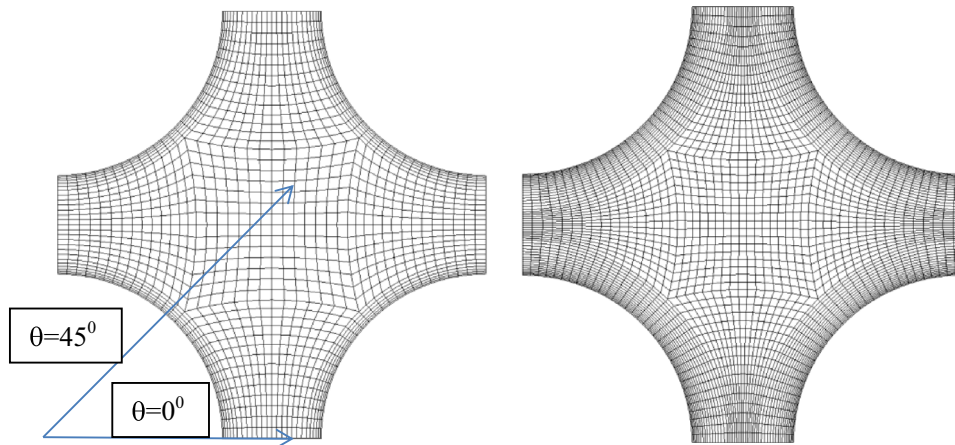


Fig. 2. Medium (left) and fine (right) grids for LES (x-y). Arrows show 0° and 45° segments.

of the domain was reduced from the PWR case to relax the meshing requirements in the axial direction. Since the distance to the onset of nucleate boiling depends on the integrated power (heat flux times rod surface area) supplied to the fluid, the heat flux was scaled accordingly; see Table 2.

The PSBT operating conditions are summarized in Table 1. The actual (reduced) operating conditions are summarized in Table 2.

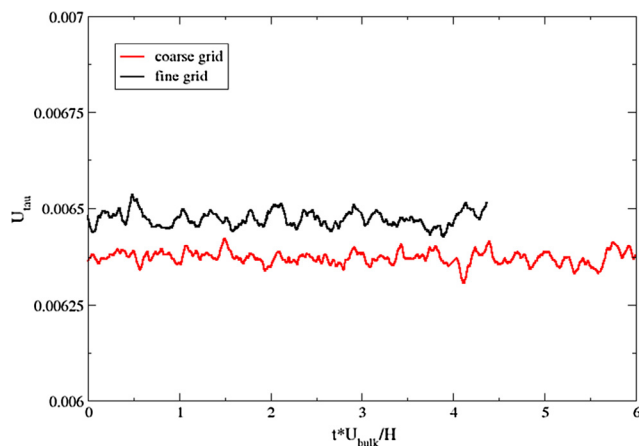


Fig. 3. Frictional velocity evolution with non-dimensional time.

4. Problem setup

4.1. Computational domain, boundary conditions & mesh

The dimensions of the simulation domain and boundary conditions are indicated in Fig. 1. The geometry features cross-sectional dimensions similar to the PSBT case; rod diameter $D = 10$ mm and pitch $P = 13$ mm. The length is reduced from 3.6 m to 1.0 m. A novel approach was used to generate proper boundary conditions for this flow. Periodic conditions were applied in the radial and circumferential directions to mimic the effect of the neighbouring rods. In the axial direction, however, a new technique has been developed to overcome this difficulty, known as the ‘Developed & Developing Flow Hybrid Approach’. It consists of first generating turbulence in a periodic domain of length $2\pi D_e$, then the resulting fluctuating (scaled to maintain the mass flow rate) field is imposed in the entire domain, recycled periodically: temperature is updated using inflow-outflow BCs. Two Body-Fitted Co-ordinate (BFC) grids were employed (Table 3): the medium one consists of $798 \times 40 \times 40$ cells providing a near-wall resolution of $y^+ \sim 0.5$ – 2.1 , which allows resolving the viscous sublayer. The second grid consists of $1600 \times 60 \times 60$ cells, providing a near-wall resolution of $y^+ \sim 0.4$ – 1.5 .

4.2. Initial conditions & simulations parameters

The initial flow conditions for the full domain were generated from an earlier flow solution obtained using cyclic inflow-outflow

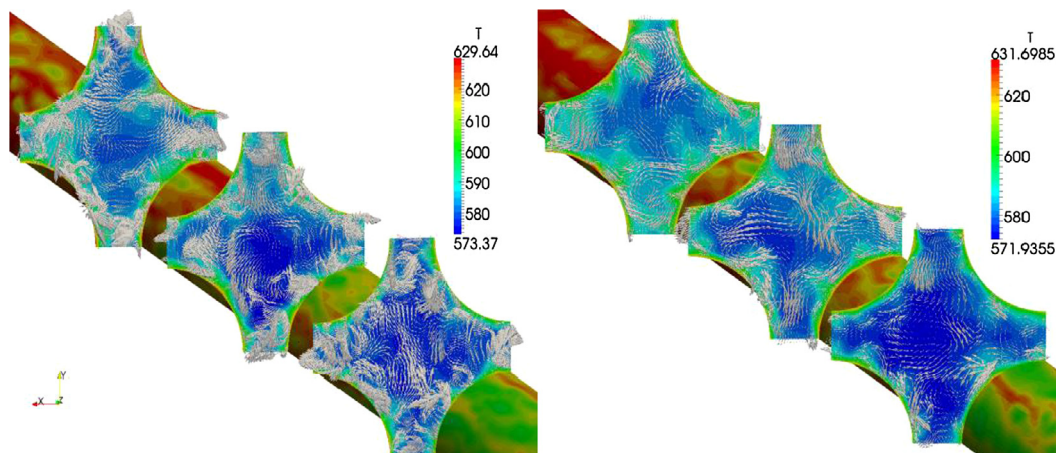


Fig. 4. Fine (left) vs. medium (right) grid: instantaneous velocities and temperature contours.

in a shorter $2\pi D_e$ long domain. During this process, to speed up the turbulent flow generation, various grids of different refinements (coarse, medium and refined) were employed in a sequential way: the solution obtained on the coarse grid is mapped into the medium one, the solution of which is then passed to the fine mesh, which at the end is transferred to the final run as an initial/inflow/outflow condition. Assuming the flow to be non-homogenous with a dominant velocity fluctuation in the flow direction, component w' (in the flow direction) fixed as the variance of u_τ . The other components were defined as $u' = 2/3w'$ and $w' = 1/3u'$. This process is

innovative; it allows generating the fluctuating field to the finest mesh (60×60 in cross section) rather fast.

The simulations were performed on the DOE's leadership super-computer TITAN located at ORNL, using 144 and 832 MPI cores for the medium and fine grids, respectively. The DSM model presented earlier was used in the context of LES. Statistical flow averaging was performed over 6 flow-through times for the medium grid and 4.5 flow-through times for the fine grid. The wall shear velocity u_τ converged to 0.0065 m/s for the fine grid and to 0.0064 m/s for the medium one, as shown in Fig. 3.

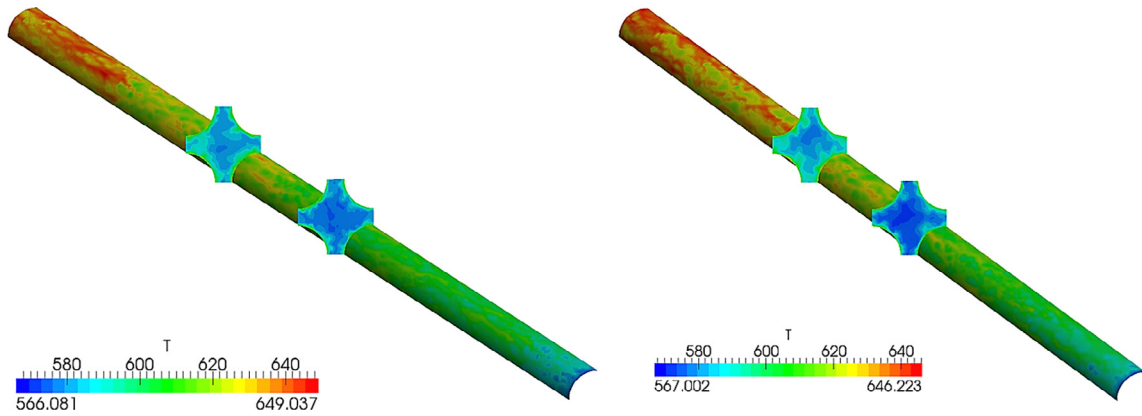


Fig. 5. Fine (left) vs. medium (right) grid: instantaneous cross-sectional velocities and temperature contours.

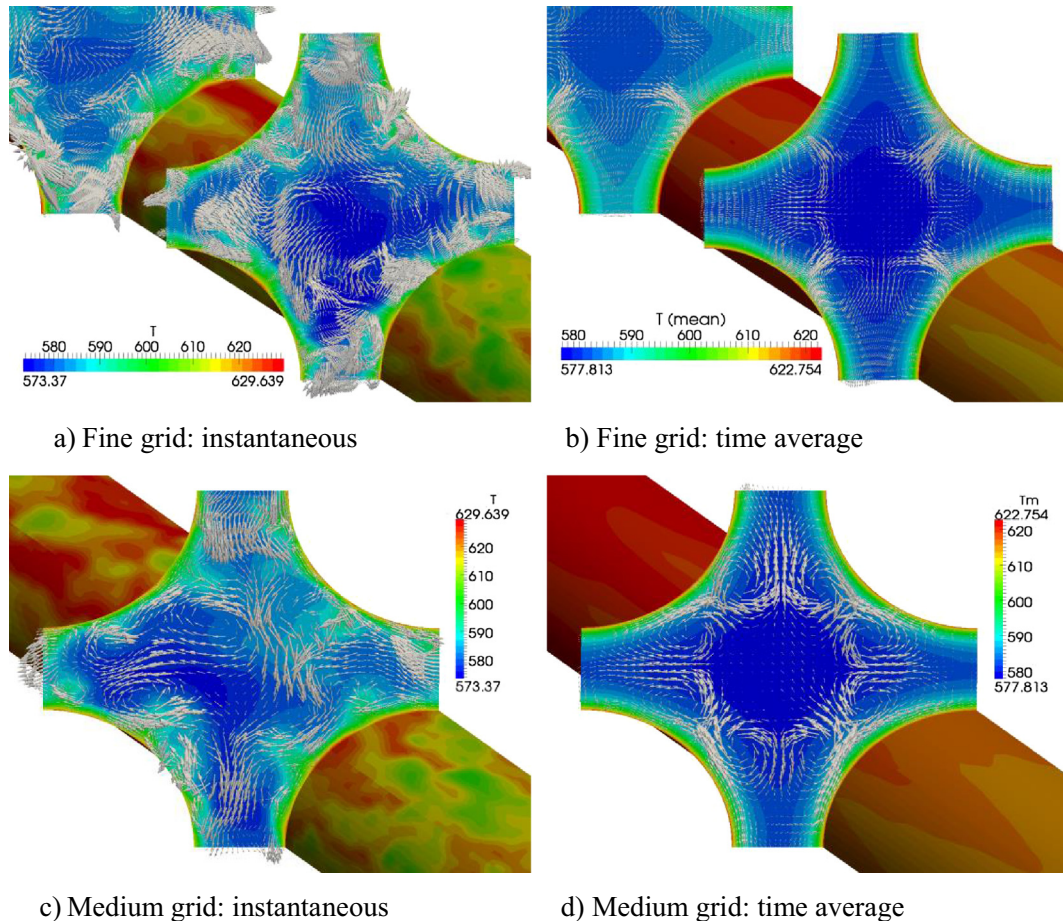


Fig. 6. Fine vs. medium resolutions: Instantaneous (a and c) and time averaged (b and d) cross-sectional velocities and temperature contours.

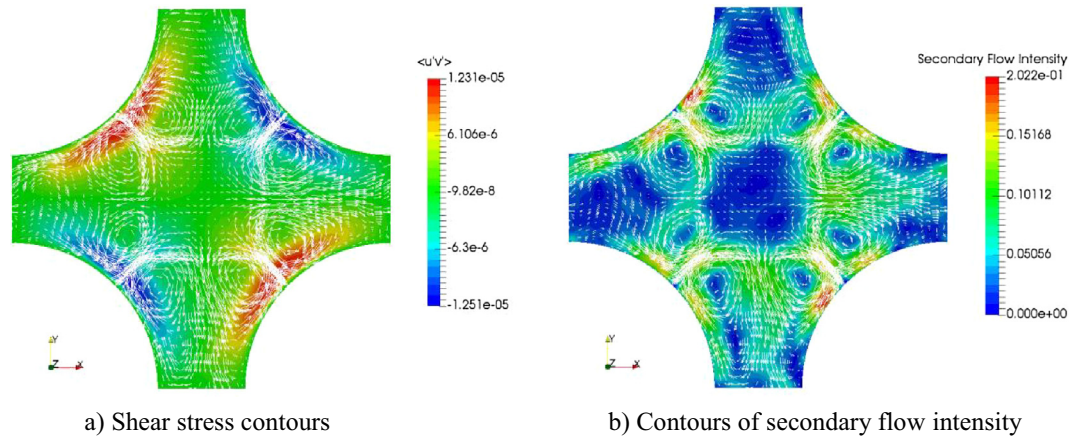


Fig. 7. Time averaged cross-sectional shear-stress and secondary-flow intensity ($\text{Abs}(\bar{U}\bar{V}/\bar{u}'\bar{v}')$) contours.

5. Simulation results

5.1. Flow structures results

The flow structure at various instances near the central area obtained for the medium and the fine grids are compared in Figs. 4 and 5. While no major differences can be observed, the cross-sectional views show more structures developing in the fine grid simulation (left panel), as was to be expected. Temperature contours on the rod surface show intermittent patches related to turbulent eddies transporting heat from the wall to the core flow. Fig. 5 in particular (scaled view) shows the space development of the thermal field along the rod on its surface; the highest values are observed in the very upper portion of the rod. The results also confirm that the 'Developed & Developing Flow Hybrid Approach' developed for the purpose works well, in that the thermal field obtained is indeed space developing in contrast to the flow field.

The secondary-flow is discussed in the context of Figs. 6 and 7, presenting instantaneous and time averaged cross-flow field and wall temperature fields. Important point to note is that the mean flow exhibits in both grid simulations a rather strong secondary flow motion, the effect of which can be perceived on the wall temperature contours, showing a patchy structure due to the intermittency of the mean and turbulent flow motions acting in tandem. Fig. 6 shows symmetric secondary-flow cells forming in the gaps. In order to quantify the strength of these cells, we introduce here a measure for the purpose in the form of the ratio of mean to turbulent cross-flow motion, referred to as the Secondary Flow Intensity (SFI), defined as: $\text{Abs}(\bar{U}\bar{V}/\bar{u}'\bar{v}')$. Our intention is to draw a map separating mean flow from turbulence dominated secondary-flow regions. The left panel of Fig. 7 showing contours of the shear stress ($\bar{u}'\bar{v}'$) in the cross flow reveals that this turbulent quantity is important in the near-wall region, as expected. The right panel indicates that the secondary flow intensity is dominated by the mean flow ($\bar{U}\bar{V}$) motion near the wall ($\text{SFI} \sim 1\text{--}2$), while the shear-induced counterpart prevails in the core flow region, where $\text{SFI} \sim 0.1\text{--}0.2$. This important result indicates that wall-to-flow heat transfer depends heavily on the secondary flow motion induced by the mean flow. The effect of these secondary-flow motions is clearly indicated by the instantaneous and time averaged temperature contours on the rod surface plotted in Fig. 8, indicating the position for saturation temperature marked by a black line. In both medium and fine-grid simulations, the line varies spatially by about 5–7% around the mean.

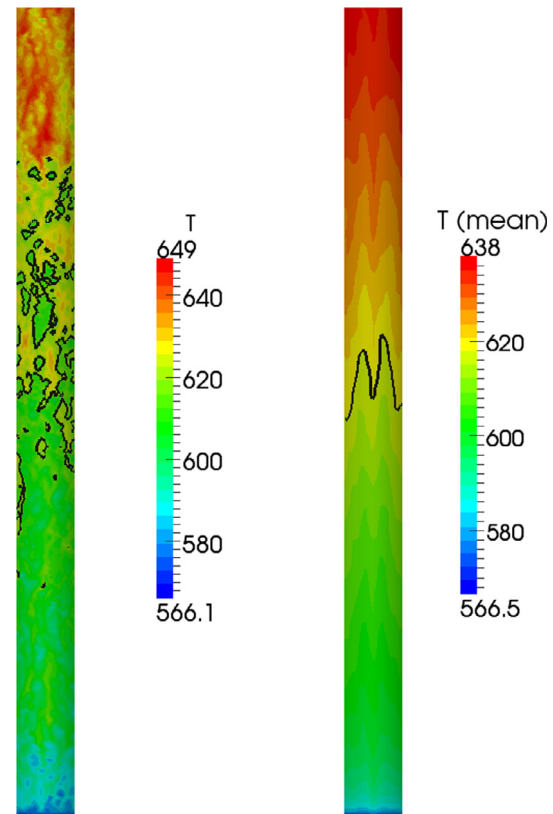


Fig. 8. Fine vs. medium resolutions (scaled domain for illustration): Instantaneous and time averaged temperature contours. The black line on the right panel indicates X_{onb} , the position of T_{sat} .

5.2. Time averaged results

Time averaged results are presented in Figs. 9–13, including flow and temperature mean and key turbulent profiles. Only fine-grid results are discussed; in most cases the medium-grid data were found globally close to the fine-grid results. Since the flow resembles turbulent flow in a pipe, use was made of available DNS data at $Re_{\tau} = 360$ [20] for comparison. The DNS data are not filtered. The difference with the pipe flow is that the present one has two azimuthal segments, a short one ($\theta = 0^\circ$) with low Re effects and a full one ($\theta = 45^\circ$) extending to the core with high Re effects (see Fig. 2). The latter one should thus return the imposed shear Reynolds number at the subchannel center point, in the form of

$y^+_{\text{centerline}} = Re_\tau$. The mean velocity profiles are plotted in Fig. 9. As explained earlier, the $\theta = 0^\circ$ segment profile achieves a lower y^+ (~ 90) than the $\theta = 45^\circ$ one. The profiles match very well the DNS data of Eggels et al. [20], with an insignificant difference in the y^+ interval 40–90. This preliminary important result pleads in favour of a high quality highly-resolved LES achieved by CFD code TransAT.

Fig. 10 presents the mean temperature profiles normalized using $\Delta T = (T_{\text{sat}} - T_{\text{in}})$ across the subchannel at various streamwise locations, for both segments: $\theta = 0^\circ$ (left panel) and $\theta = 45^\circ$ (right panel). The plots reveal deviations very close to the wall, pointing to different shapes and slopes of the thermal boundary layer, which seems to develop to about $0.3R$ in the $\theta = 0^\circ$ segment, against $\sim 0.2R$ for the $\theta = 45^\circ$ segment. As was reported already by Ikeno and Kajishima [12] from their simulations, while the $\theta = 45^\circ$ section exhibits a full turbulent flow profile, the $\theta = 0^\circ$ segment results reveal strong low-Re effects, a characteristics feature specific to narrow gap zones in subchannel flows.

Fig. 11 compares the averaged flow-direction normal stresses ($\overline{w'w'}$) profiles to the pipe-flow DNS of Unger & Friedrich [21] and Eggels et al. [20]. Here again we plot the 0° low-Re segment and the 45° high-Re core-flow one. The comparison shows the same level of agreement as obtained by Ikeno and Kajishima [12] using LES, too. The fine-grid simulation provides a very good match in terms of trend with DNS, although our case is a higher Re case and as such it should return a higher peak in the r.m.s value at $y^+ \sim 15$, followed by gradual decay towards unity in the range $120 < y^+ < 160$. The mean profiles of the $\overline{v'v'}$ stress component show values that are one order of magnitude smaller than $\overline{w'w'}$; these are not discussed here. Fig. 12 presents the turbulent

heat-flux ($\overline{w'\theta'}$) profiles for the two segments. The peak value is also obtained at $y^+ \sim 15$, but the profile now exhibits a sharp drop in the $y^+ < 100$ range, before plateauing to a low value. Another important measure is the temperature variance ($\overline{\theta'\theta'}$), which is plotted in Fig. 13 for both segments, at various cross-flow locations. The 45° segment results shown in the right panel exhibit variations in the normalized (by $T_{\text{sat}} - T_{\text{in}}$) temperature variance with elevation, which is not the case in the 0° low-Re segment (left panel). This may be an artefact of normalization; the profile could have shown a self-similar behavior if it were normalized by the average wall temperature. Like the turbulent heat flux profile, the variance profile also exhibits a sharp drop in the $y^+ < 100$ range, before plateauing to a lower value. Further, the results indicate that possible thermal effects on the rod could be expected in

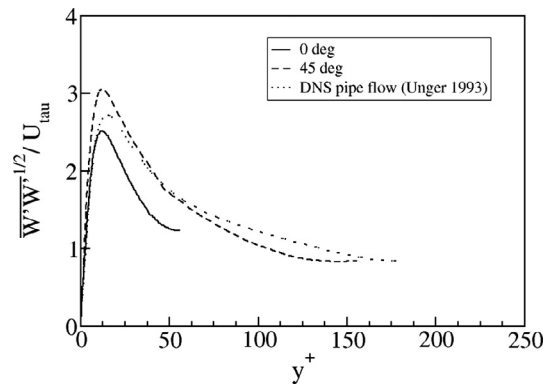


Fig. 11. Averaged normal-stresses profiles ($\overline{w'w'}$) at 0° & 45° .

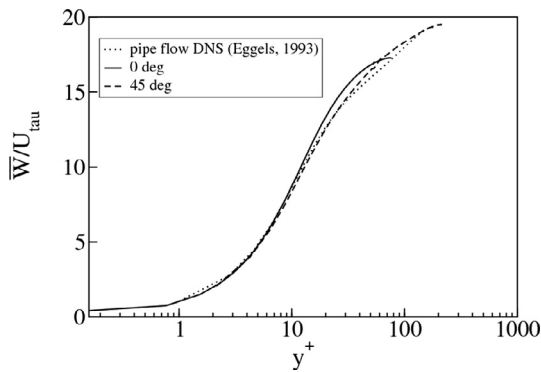


Fig. 9. Mean velocity profiles across the subchannel (0° & 45°) compared to the DNS of Eggels et al. [20].

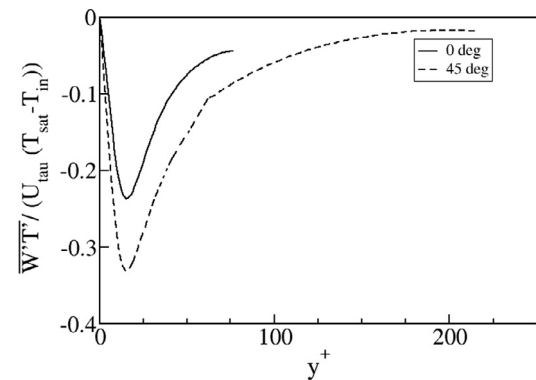


Fig. 12. Averaged heat flux profiles ($\overline{w'\theta'}$) at 0° & 45° .

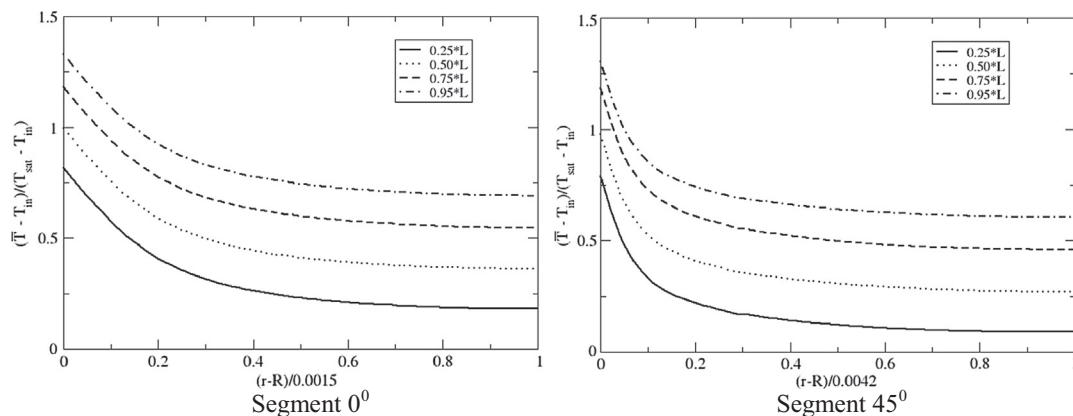


Fig. 10. Mean temperature profiles across the subchannel at various streamwise locations.

the 45° segment area, where turbulent effects are the most perceivable. The peak value of this quantity is twice larger in the 45° segment than in the narrow gap.

5.3. Energy spectra results

Results obtained with the medium grid are compared in Fig. 14. Overall the same trend is observed as to the three velocity components, albeit some subtle differences do pertain as to the decay rate. As was to be expected from the flow statistics, energy carried out by the largest scales ($f < 1$ Hz) is essentially concentrated in the axial velocity component W, although the other two components carry similar amounts in the high-frequency range ($f > 1$ Hz), with a decay behavior smoother in the flow directions than the other directions. The result discussed in Fig. 15 is interesting in that it depicts other phenomena occurring at the highest-frequency range: The decay in the smallest scales range seems indeed to be rather peculiar, exhibiting a sharp drop in the range $10 < f < 25$ –30 Hz, before adjusting to the $-5/3$ slope in the interval $30 < f < 700$ Hz. This peculiar behavior was actually observed in the experiments conducted by Rehme [5], who pointed out to the effect of

large-scale structures. The absence of a clear peak in the power spectrum translating the coherent pulsations as was found by Rehme [5] and Meyer [7] in the low frequency range (< 10 Hz) is due to the limitation of size of the domain and periodic conditions applied in this LES context.

5.4. Global parameters results

Global parameters results are presented in Table 4. The LES results are compared here to existing analytical and experimental correlations. The pressure drop between medium and fine grid is accurate to 2.2% and 5% compared to the correlation. As to the heat transfer coefficient (HTC), there are uncertainties for the case of interest, which in fact belongs to the ‘transitional cases regime’, according to Incropera and DeWitt [4], for which the correlations, in particular the Colburn one (or Dittus-Boelter), could give up to 25% error. When accounting further for the effect of neighbouring rods using the Weisman correction (here $\Psi = 1.826p/D - 1.043 = 1.33$), the deviations between LES and correlation is high, and is precisely 33%. If this correction is not accounted for, the LES results (fine grid in particular) are comparable to the Colburn correlation,

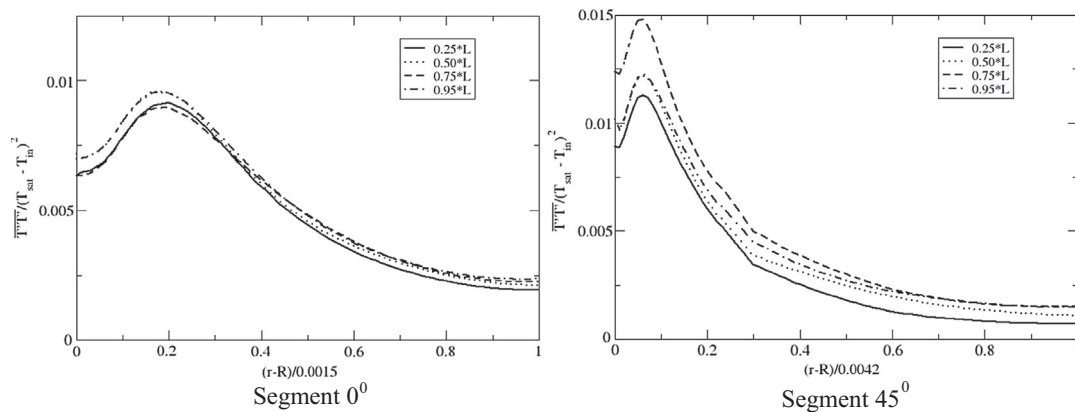


Fig. 13. Temperature variance profiles ($\overline{\theta'\theta'}$) at various streamwise locations of the subchannel.

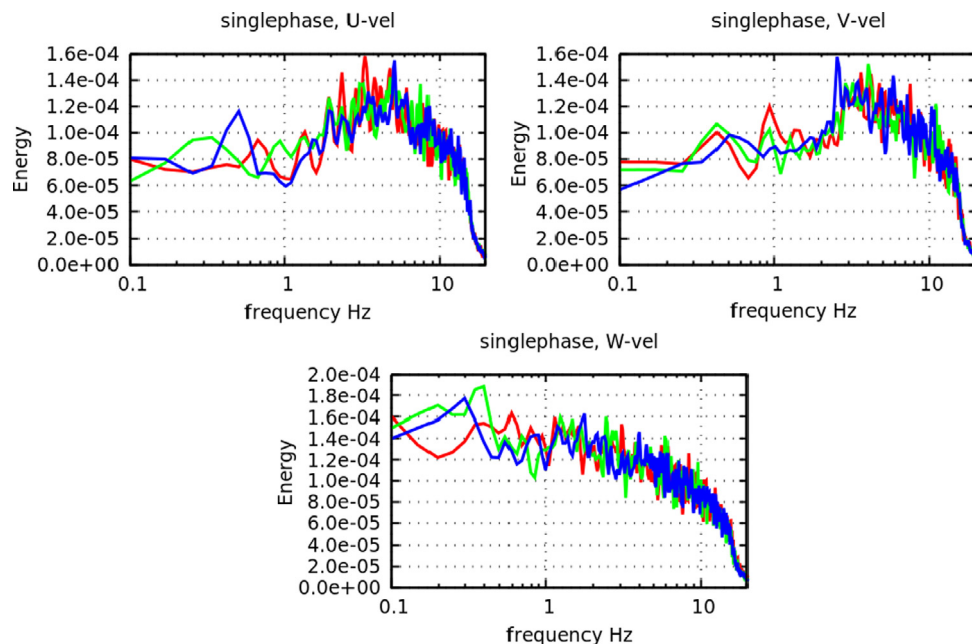


Fig. 14. Low-frequency PSD of U, V and W at various locations ($z/L = 0.55, 80$ and 95).

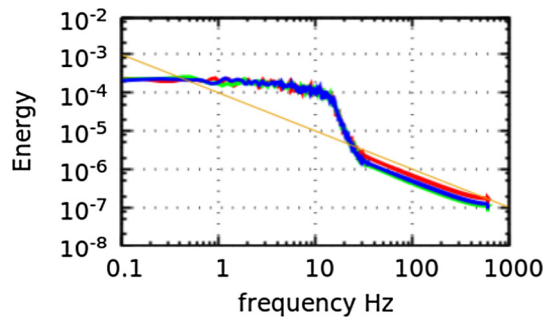


Fig. 15. Low- & high-frequency PSD of W velocity at various locations ($z/L = 0.55$, 80 and 95).

Table 4

Test case 2 operating flow conditions.

Quantity	Med. grid	Fine grid	Analytical/Exp.
Pressure drop ΔP [Pa]	10.223	10.52	10.0
Heat transfer coefficient (HTC) at X_{ONB} [$\text{kW/m}^2 \text{K}$]	1.495	1.535	1.62 (Colburn) 2.16 (Colburn-W) 1.44 (Gnielinski) 1.99 (Gnielinski-W) 1.50 (Petukov) 2.0 (Petukov-W)
Distance to X_{ONB} [m]	Min-max 0.49–0.57	Min-max 0.49–0.6	0.59 (Colburn) 0.79 (Colburn-W)
Thermal entry length [m]	Min-max 0.21–0.28	Min-max 0.21–0.29	0.29–0.46

* W means with the Weisman (1959) correction factor.

within $\sim 5\%$. With more sophisticated correlations e.g. the Gnielinski and Petukov (see [4]), the analysis changes, in that the LES data are 6% than Gnielinski's correlation and 1.9% only than Petukov's one.

The distance to the onset of boiling is questionable in the same way, since it is directly based on the HTC correlation employed (here we took the Colburn one only). The simulation results are within a few percent's deviations from the Colburn correlation, but 24–35% off the Colburn–Weisman variant, which is in line with the HTC deviations reported. Finally, as stated previously, there is no such a constant line indicating X_{ONB} since the simulations have clearly shown that the effect of the secondary flow motion makes it rather undulating by 5–7% around the mean.

6. Conclusions

The paper reports a detailed simulation analysis of turbulent convective flow upward along the heated rods of a PWR subchannel using the CFD/CMFD code TransAT. Boiling effects were not considered. Turbulence was predicted using highly-resolved LES with the fine grid consisting in 6 million cells, for which the subgrid scale viscosity produced by the model was found to be of marginal effect. A novel technique known as the 'Developed & Developing Flow Hybrid Approach' has been developed, which consists in generating turbulence along the rod in a periodic domain, assuming developed flow conditions, while treating the temperature as a space-developing field. The comparison of the LES results with existing DNS of pipe flow shows a very good agreement as to first-order turbulence statistics. Higher-order statistics were found to require much more simulation samples to achieve ergodic flow statistics.

The results including key features specific to rod bundles were thoroughly discussed, including low-Re effects in the narrow gap

zone. The simulations revealed important information on the mechanism of secondary-flow motion and its intensity, which has been partitioned into mean and turbulent contributions. It is shown that the mean-flow contributes mostly to the secondary flow near the wall, while the turbulent part dominates the mechanism in the core flow region. The secondary-flow motion induced by the mean flow can thus be responsible for most of the heat transfer from the wall to the flow field.

The comparison with correlations as to engineering parameters show that excellent results are obtained for pressure drop, but raise important questions as to the validity of heat-transfer coefficient correlations in this transitional regime, and indirectly the location of onset of nucleate boiling. A data basis has been generated for RANS model comparison, and can be made available for use to address the predictive performance of these models. The simulation campaign has since then been extended to boiling heat transfer.

Conflict of interest

I hereby testify that there is no conflict of interest to invoke regarding the content of this paper.

Acknowledgements

This work was financially supported by the US Department of Energy through the CASL project (Subcontract 4000107101). The simulations were performed on TITAN supercomputer located at ORNL Oak Ridge, TN, USA. The authors would like to acknowledge the support of the MIT team: Prof. J. Buongiorno and Dr D. Chatzikyriakou. The simulations were conducted and monitored by Daniel Caviezel.

References

- [1] J.G. Collier, J.R. Thome, *Convective Boiling and Condensation*, third ed., Oxford University Press, 1996.
- [2] TransAT, ASCOMP software package, 2017. <<http://www.ascomp.ch/transat>>.
- [3] A. Rubin et al., OECD/NRC Benchmark based on NUPEC PWR subchannel and Bundle Tests (PSBT), NEA/NSC/DOC, 2010.
- [4] H. Incropera, J. DeWitt, *Intl. Heat Transfer*, third ed., Wiley & Sons, 1996.
- [5] K. Rehme, The structure of turbulence in rod bundles and the implications on natural mixing between the subchannels, *Int. J. Heat Mass Transfer* 35 (2) (1992) 567–581.
- [6] D.S. Rowe, B.M. Johnson, J.G. Knudsen, Implications concerning rod bundle crossflow mixing based on measurements of turbulent flow structure, *Int. J. Heat Mass Transfer* 17 (1974) 407–419.
- [7] L. Meyer, From discovery to recognition of periodic large scale vortices in rod bundles as source of natural mixing between subchannels—a review, *Nucl. Eng. Des.* 240 (6) (2010) 1575–1588.
- [8] W.J. Seale, Measurements and predictions of fully developed turbulent flow in a simulated rod bundle, *J. Fluid Mech.* 123 (1982) 399–423.
- [9] V. Vonka, Measurement of secondary flow cortices in a rod bundle, *Nucl. Eng. Des.* 106 (1988) 191–207.
- [10] D. Chang, S. Tavoularis, Simulations of turbulence, heat transfer and mixing across narrow gaps between rod-bundle subchannels, *Nucl. Eng. Des.* 238 (1) (2008) 109–123.
- [11] T. Ikeno, T. Kajishima, Decay of swirling turbulent flow in rod-bundle, *J. Fluid Sci. Technol.* 1 (1) (2006) 36–47.
- [12] T. Ikeno, T. Kajishima, LES of turbulent flow in subchannel and analysis of driving force of secondary flow, *J. Fluid Sci. Technol.* 2 (2) (2007) 480–489.
- [13] T. Ikeno, T. Kajishima, Analysis of dynamical flow structure in a square arrayed rod bundle, *Nucl. Eng. Des.* 240 (2) (2010) 305–312.
- [14] E. Merzari, H. Ninokata, E. Baglietto, Numerical simulation of flows in tight-lattice fuel bundles, *Nucl. Eng. Des.* 238 (7) (2008) 1703–1719.
- [15] H. Ninokata, E. Merzari, A. Khakim, Analysis of low Reynolds number turbulent flow phenomena in nuclear fuel pin subassemblies of tight lattice configuration, *Nucl. Eng. Des.* 239 (5) (2009) 855–866.
- [16] D. Chatzikyriakou, J. Buongiorno, D. Caviezel, D. Lakehal, DNS and LES of turbulent flow in a closed channel featuring a pattern of hemispherical roughness elements, *Int. J. Heat Fluid Flow* 53 (2015) 29–43.
- [17] P. Sagaut, *Large Eddy Simulation for Incompressible Flows: An Introduction*, Springer Pubs., 2005.

- [18] P. Moin, K. Squires, W. Cabot, S. Lee, A dynamic sub grid-scale model for compressible turbulence and scalar transport, *Phys. Fluids* 3 (11) (1991) 2746–2757.
- [19] S.H. Peng, L. Davidson, Large eddy simulation for turbulent buoyant flow in a confined cavity, *Int. J. Heat Fluid Flow* 22 (3) (2001) 323–331.
- [20] J.G.M. Eggels, F. Unger, M.H. Weiss, J. Westerweel, R.J. Adrian, R. Friedrich, F.T. M. Nieuwstadt, Fully developed turbulent pipe flow: a comparison between direct numerical simulation and experiment, *J. Fluid Mech.* 268 (1994) 175–209.
- [21] F. Unger, R. Friedrich, Large eddy simulation of fully-developed turbulent pipe flow, in: *Proc. 8th Symp. on Turbulent Shear Flows*, Sep. 1991, Munich, Germany, 1991, 19/3/1–19/3/6.